USING ANISOTROPIC DIFFUSION FOR COHERENCE ESTIMATION

François Aspert[1], Alessio Cantone[2], Jean-Philippe Thiran[1], and Paolo Pasquali[2]

[1]*Ecole Polytechnique Fédérale de Lausanne (EPFL), CH-1015 Lausanne, SWITZERLAND*
[2]*Sarmap S.A., Cascine di Barico, 6989 Purasca, SWITZERLAND*

ABSTRACT

In this paper we will present a new coherence estimation technique for SAR interferometry products that adapts the estimation window size and shape during processing. This is of particular interest for sensors with medium spatial resolution, like the ASAR WS mode, where the estimator shall cope with the spatial variability of the targets in the imaged area. This method is designed to remove low coherence magnitude bias while keeping a good spatial resolution. Finally, this new approach will be compared to an existing algorithm for quantifying resulting quality improvement.

1. INTRODUCTION

In synthetic aperture radar (SAR) interferometry (In-SAR), the use of the coherence measure is required in order to achieve a precise estimation of the corresponding interferogram quality. It is therefore a crucial value as it enables the reliable and accurate extraction of displacement and elevation information [1] [2] as well as performing land-use classification tasks [3] [4]. However, existing estimators are biased towards higher values especially for low coherence magnitudes. Such a bias can be removed by increasing the number of samples taken into account during coherence computation, provided that the scene is stationary in mean. These conditions tend to prevent the use of large windows to compute the estimation and limits the overall resulting accuracy. Our assumption here is to use the backscattering coefficients of amplitude images [5] to identify the single objects that are ergodic.

The proposed technique uses anisotropic diffusion to approximate local stationary processes and being less sensitive to unwanted amplitude variations due to speckle in the sources interferogram images. Such a technique aims at providing an edge sensitive filtering so as to preserve natural discontinuities that are present in the image. In this manner, we are able estimate coherence using these regularized regions while enabling accurate non-stationarity detection. The chosen algorithm has the property of being fully applicable to vector-valued images with a significant result improvement in resulting filtering quality when images from same location are pro-

vided. In the case of Interferometry, source amplitude images can thus be exploited together so that it takes into account independent realizations of the speckle. Different measures will be shown in order to prove the accuracy of our methods onto two different data sets (originating from ERS-1 and ENVISAT-WS)

First in Section 2, we will present the theory related to coherence estimation problem. Then in Section 3, we will introduce the basic concept of anisotropic filtering and its vector-valued counterpart. In section 4, three different (but complementary) methods for coherence estimation are presented. Results and qualitative observations are outlined in Section 5. Finally, conclusions and future work will be discussed in Section 6.

2. COHERENCE ESTIMATION

The complex coherence has been defined in [6] as the correlation between two complex signals. If v_1 and v_2 are two zero-mean complex random stationary processes, the coherence magnitude can be expressed as:

$$\gamma = \left| \frac{E(v_1 \cdot v_2^*)}{\sqrt{E(|v_1|^2) \cdot E(|v_2|^2)}} \right|, \qquad (1)$$

where * denotes the complex conjugate and $E(v)$ is the ensemble average operator. The sample coherence estimator (maximum-likekihood estimator) is then [7] [8]:

$$\hat{\gamma} = \left| \frac{\sum_{i=0}^{N} v_{1i} \cdot v_{2i}^*}{\sqrt{\sum_{i=0}^{N} |v_1|^2 \sum_{i=0}^{N} |v_2|^2}} \right|, \qquad (2)$$

computed over N independent observations of the processes involved. This estimator is asymptotically unbiased. Nevertheless, if the ensemble average of Eq. 1 can be replaced by the time average in Eq. 2, it is in practice difficult to estimate as it requires a large number of acquisitions of the same pixel under the same conditions to ensure processes stationarity and mean ergodicity.

Therefore, in order to obtain a tailored estimator for coherence for InSAR products we can substitute the ensemble average by a spatial average within stationary regions.

The sampled estimator becomes [9]:

$$\hat{\gamma}_{i,j} = \frac{|\sum_{m=0}^{M} \sum_{n=0}^{N} v_{1(m,n)} \cdot v_{2(m,n)}^*|}{\sqrt{\sum_{m=0}^{M} \sum_{n=0}^{N} |v_{1(m,n)}|^2 \sum_{m=0}^{M} \sum_{n=0}^{N} |v_{2(m,n)}|^2}}.$$
(3)

Here, for each pixel of coordinates (i, j), the coherence is computed by spatially averaging pixels values within a finite window with a fixed size $M \times N$ centered in (i, j). For InSAR, the two images differs by a deterministic phase ϕ. If this phase is not constant inside a given window, it can induce a bias in the estimator. However, it is very likely that this phase is not constant (especially in mountainous areas where steep slopes are imaged), it has to be compensated. Eq. 4 gives the expression for terrain slope compensated coherence estimator.

$$\hat{\gamma} = \frac{|\sum_{m=0}^{M} \sum_{n=0}^{N} v_{1(m,n)} \cdot v_{2(m,n)}^* \exp^{-j\phi(m,n)}|}{\sqrt{\sum_{m=0}^{M} \sum_{n=0}^{N} |v_{1(m,n)}|^2 \sum_{m=0}^{M} \sum_{n=0}^{N} |v_{2(m,n)}|^2}}.$$
(4)

But, if such a method is capable of removing the bias for low-coherence zones, it requires an important number of samples to be taken into account, thus lowering the overall spatial resolution. Moreover, within a given window, the scene is not ensured to be stationary, leading to a false estimation of the coherence. In [9], a tentative for estimating coherence using images intensity and variable windows size is introduced. However, the determination of the optimal size remains problematic as it is difficult to choose which pixels to include in the final estimation.

3. ANISOTROPIC DIFFUSION

3.1. Single Image Diffusion Filtering

First introduced in [10] for single optical images, this particular type of filtering allows a high level of regularization in homogenous areas while preserving the relevant features. For a continuous image, diffusion on image $\mathbf{I}$ may be enacted by the partial differential equation 5:

$$\frac{\partial \mathbf{I}}{\partial t} = \text{div}[c(\|\nabla \mathbf{I}_\sigma\|) \cdot \nabla \mathbf{I}_\sigma],$$
(5)

where ∇ is the gradient , div is the divergence operator, and c, the conduction coefficient is a matrix of diffusion coefficients of the same size as $\mathbf{I}$. c is designed to be a non-linear function of the smoothed image gradient magnitude $\|\nabla \mathbf{I}_\sigma\|$. The design of c if extremely important. Black [11] made an in-depth study of the design of c and link the Perona diffusivity function to the weighting functions of robust statistical estimation. This led to another diffusivity function from the Tukeys biweight:

$$c(\|\nabla \mathbf{I}_\sigma\|, \lambda) = \begin{cases} \frac{1}{2}[1 - (\frac{\|\nabla \mathbf{I}_\sigma\|}{\lambda})^2]^2 & \|\nabla \mathbf{I}_\sigma\| \leq \lambda \\ 0 & \text{otherwise} \end{cases}$$
(6)

Where λ refers to the sensitivity parameter and is set up in an automated way using fixed size windows in order to

have a spatially varying threshold and be more sensitive to potential image variations. But, the main drawback of nonlinear diffusion is that such a technique leaves the edge features unfiltered. To overcome this situation, Weickert [12] [13] introduced edge-direction sensitive diffusion. The amount of diffusion is controlled by a matrix $\mathbf{D}$ (also called diffusion tensor) of values specifying the diffusion importance in the features direction. The anisotropic diffusion is thus described by Eq. 7.

$$\frac{\partial \mathbf{I}}{\partial t} = \text{div}[\mathbf{D}(\nabla \|\mathbf{I}_\sigma\|) \cdot \nabla \mathbf{I}_\sigma], \qquad \mathbf{D} = \begin{pmatrix} a & b \\ b & c \end{pmatrix},$$
(7)

where,

$$a = \phi_1 \cos^2 \alpha + \phi_2 \sin^2 \alpha, \qquad (8)$$
$$b = (\phi_1 - \phi_2) \sin \alpha \cos \alpha, \qquad (9)$$
$$c = \phi_1 \sin^2 \alpha + \phi_2 \cos^2 \alpha. \qquad (10)$$

where α is the direction of the gradient (maximum variation angle). ϕ_1 controls the diffusion along the gradient whereas ϕ_2 will be in charge of the filtering process perpendicular to this gradient. Therefore, ϕ_1 h will be chosen to behave in the same way as c in nonlinear diffusion. ϕ_2 will be fixed to a constant value as we require edges to be smoothed uniformly.

3.2. Vector-Valued Diffusion Filtering

The difference with the work done in [14] lies in the diffusion amount computation which is no longer varying with a single-image gradient. The choice is made to measure the gradient using the whole set of images. The most natural choice is then to use the reliable formulation for gradient computation with vector data stated in [15] used by Sapiro [16] which takes the gradient as a two dimensional manifold embedded in $\Re^m$. We obtain for the multi-temporal image sequences the following First Fundamental Form (FFF):

$$d\mathbf{f}^2 = \begin{pmatrix} dx \\ dy \end{pmatrix}^{\mathbf{T}} \begin{pmatrix} g_{11} & g_{12} \\ g_{12} & g_{22} \end{pmatrix} \begin{pmatrix} dy \\ dy \end{pmatrix}$$
(11)

Where,

$$\begin{cases} g_{11} = \sum_{i=1}^{m} \nabla \mathbf{I}_{\sigma,(i,x)}^2, \\ g_{12} = \sum_{i=1}^{m} \nabla \mathbf{I}_{\sigma,(i,x)} \nabla \mathbf{I}_{\sigma,(i,y)}, \\ g_{22} = \sum_{i=1}^{m} \nabla \mathbf{I}_{\sigma,(i,y)}^2. \end{cases}$$
(12)

Where $\mathbf{I}_{\sigma,(i,x)}^2$ and $\mathbf{I}_{\sigma,(i,y)}^2$ stands respectively for gradient estimation along columns and lines. The direction and magnitude of the maximum and minimum rate of change corresponding to the computed gradient directions can be then extracted from the FFF eigenvalues and eigenvectors

in Eq. 11. Finally, Eq. 13 gives the practical framework of the anisotropic diffusion process.

$$\begin{cases} \frac{\partial \mathbf{I_1}}{\partial t} & = & \mathrm{div}[\mathbf{D} \cdot \nabla \overrightarrow{\mathbf{I}}] \\ & \vdots & \\ \frac{\partial \mathbf{I}_n}{\partial t} & = & \mathrm{div}[\mathbf{D} \cdot \nabla \overrightarrow{\mathbf{I}}] \end{cases} \qquad (13)$$

Where $\overrightarrow{\mathbf{I}}$ corresponds to the whole image sequence and $\mathbf{I}_i$ is the ith image in the sequence. Therefore, each image is filtered separately using the global sequence information, taking into account features from all images.

3.3. Discretization schemes

Since the equation presented in Equation 5 holds for continuous images, one have to discretize it in space and in time in order to apply it to digital images while preserving the consistency and accuracy of the solution. Here, for both space and time, finite difference methods will be used. For discretization in time, finite differences approximates $\frac{\partial \mathbf{I}}{\partial t}$ by $\frac{\mathbf{I}^{t+1} - \mathbf{I}^t}{\nu}$ where ν stands for the discrete time step. Scharr [17] proved that for tensor diffusion, an 8-element discretization stencil was consistent and accurate. If the concerned pixel is (i, j). Then on a square grid, we can extract the space discretization stencil shown in Fig. 1.

$\frac{-b_{i-1,j}-b_{i,j+1}}{4}$	$\frac{c_{i,j+1}+c_{i,j}}{2}$	$\frac{b_{i+1,j}+b_{i,j+1}}{4}$
$\frac{a_{i-1,j}+a_{i,j}}{2}$	$-\frac{a_{i-1,j}+2a_{i,j}+a_{i+1,j}}{2} - \frac{c_{i,j-1}+2c_{i,j}+c_{i,j+1}}{2}$	$\frac{a_{i+1,j}+a_{i,j}}{2}$
$\frac{b_{i-1,j}+b_{i,j-1}}{4}$	$\frac{c_{i,j-1}+c_{i,j}}{2}$	$\frac{-b_{i+1,j}-b_{i,j-1}}{4}$

Figure 1. 3x3 discretization stencil

4. ANISOTROPIC COHERENCE

In this section, we present two different approaches to solve the problem of estimating the coherence magnitude using two power images and their resulting complex interferogram. The principal philosophy is to identify or approximate homogenous (and thus stationary) regions within available images. Indeed, if these regions appear to be sufficiently large, it will provide a reliable basis of pixels for using Eq. 4 and compute an effective estimation of γ.

4.1. Amplitude driven diffusion

The first method is designed to identify the homogenous regions using source amplitude images discontinuities. In such a case, the vector-valued definition of the gradient (Eq. 11) can be here used to combine different sources images of the same scene (even multi-temporal) to obtain an improved gradient map based on images redundancies. From Fig. 1, we know that during the diffusion process, each pixel of the image will be averaged by a linear combination of each surrounding pixel with the coefficients computed using Eq. 9-10. These diffusion coefficients are computed with respect to the image geometry. That means that each pixel will be averaged with neighbors possessing similar backscattering characteristics rather than those from different areas.

We propose here to filter each image involved in the coherence computation according to 13. We will further refers to this method as Amplitude Driven Diffusion (ADD). In the case of InSAR data, the diffusion Equation is stated as follows:

$$\begin{cases} \frac{\partial \mathbf{S_1}}{\partial t} & = & \mathrm{div}[\mathbf{D}(S_1, S_2) \cdot \nabla(S_1, S_2)] \\ \frac{\partial \mathbf{S_2}}{\partial t} & = & \mathrm{div}[\mathbf{D}(S_1, S_2) \cdot \nabla(S_1, S_2)] \\ \frac{\partial \mathbf{I}}{\partial t} & = & \mathrm{div}[\mathbf{D}(S_1, S_2) \cdot \nabla(S_1, S_2)] \end{cases} \quad (14)$$

Where S_1, S_2 are the source amplitude images and I the scene flattened interferogram. Since each image will be diffused according to the same parameters with respect to the ground topography, the stationary hypothesis required in Eq. 4 holds. The filtered amplitude images and filtered complex interferogram can then be directly used in Eq. 4 for coherence estimation. Fig. 2 summarizes a single step of ADD.
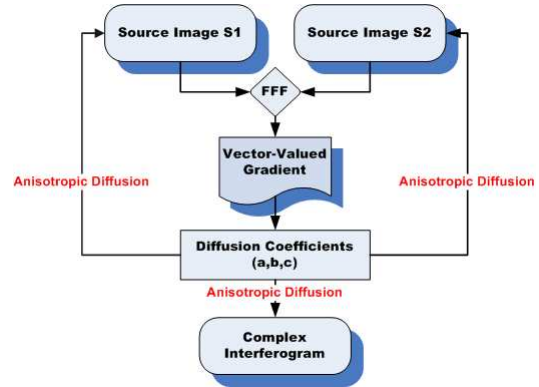

Figure 2. Amplitude Driven Diffusion

4.2. Boxcar Driven Diffusion

The goal here is still to identify homogenous regions. But here it is no longer done with amplitude image intensities but rather from a basic 3×3 boxcar coherence estimation map. Indeed, in [18], it has been proved that a "rough" estimation using small windows size can be used as a good starting point for coherence estimation. The use of such small windows prevents from averaging pixels belonging to different regions. However, for low coherence values, it has the major drawback of not using enough samples and provides a biased estimation. But, it contain some

useful information about the image geometry when inhomogeneous coherence zones appear within homogenous backscatter areas. Therefore the Boxcar map convey a different but complementary information from amplitude images.

What we propose here is to follow the framework set-up in Section 4.1. The major modification with ADD is that diffusion coefficients describing image discontinuities (named here a,b and c) are extracted using a simple centered finite difference discretization scheme directly from boxcar estimation map. We will further refer to this technique as Boxcar-Driven Diffusion (BDD).Finally, the diffusion equation described in Eq. 14 becomes:

$$\left\{ \begin{array}{rcl} \frac{\partial \mathbf{S}_1}{\partial t} & = & \mathrm{div}[\mathbf{D}(I) \cdot \nabla(I)] \\ \frac{\partial \mathbf{S}_2}{\partial t} & = & \mathrm{div}[\mathbf{D}(I) \cdot \nabla(I)] \\ \frac{\partial \mathbf{I}}{\partial t} & = & \mathrm{div}[\mathbf{D}(I) \cdot \nabla(I)] \end{array} \right. \quad (15)$$

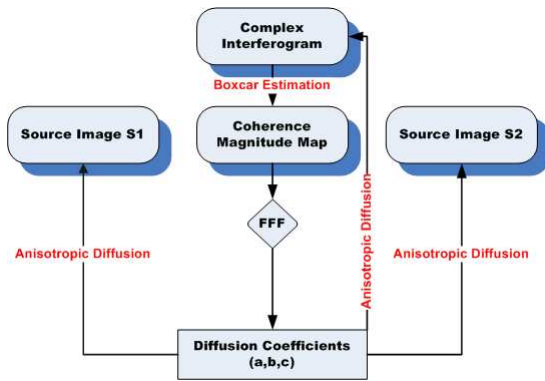Figure 3 summarizes a single step of BDD scheme.

Figure 3. Amplitude-Boxcar Driven Diffusion

4.3. Boxcar-Amplitude Methods Combination

What we propose here is an original combination of the two methods introduced before in Sec. 4.1 and 4.2. Indeed, when trying to identify homogenous areas, two main cases have to be distinguished:

- Type 1: Homogenous (or very similar) backscattering coefficients areas can have inhomogeneous coherence.

- Type 2: Homogenous coherence magnitude areas can have inhomogeneous backscattering coefficients.

With ADD we are able to handle cases of type 2. But even if it is not precise enough to provide a reliable estimation for small features, it will perform well in low gradient magnitude areas such as water. Conversely, with BDD, we can discriminate zones that appear very similar in terms backscaterring coefficient. However, it is very likely that it will lead to formation of high coherence artifacts where boxcar estimation areas is not reliable (water areas). Therefore and in order two fulfill the

aformentionned requirements, we propose a new contribution which ultimately allows to handle both of these criteria. The final coherence $\tilde{\gamma}$ is computed as:

$$\tilde{\gamma} = \left\{ \begin{array}{ll} \max(\hat{\gamma}_{\mathrm{ADD}}, \hat{\gamma}_{\mathrm{BDD}}) & \hat{\gamma}_{\mathrm{ADD}} > 0.5, \hat{\gamma}_{\mathrm{BDD}} > 0.5 \\ \min(\hat{\gamma}_{\mathrm{ADD}}, \hat{\gamma}_{\mathrm{BDD}}) & \mathrm{otherwise}, \end{array} \right.$$

$$(16)$$

where $\hat{\gamma}_{\mathrm{ADD}}$ and $\hat{\gamma}_{\mathrm{BDD}}$ denote the coherence estimation obtained respectively with ADD and BDD techniques.

5. EXPERIMENTS AND RESULTS

In this section we present the different results obtained using ADD, BDD and their combination. Our first dataset is composed of two ERS amplitude images and their corresponding phase compensated interferogram from the Bienne region (Switzerland). The working cut is an area representing a part of Bienne and Neuchâtel (small portion) lakes and their coastal zone. The second one is composed of two ENVISAT-WS power images and their corresponding flattened interferogram.

For all the testing involving diffusion that have been carried out, we used 120 iterations of the diffusion algorithm, a median-based threshold (λ) estimation computed over 100×100 non-overlapping windows and an anisotropy parameter $\phi_2 = 0.2$.

In Figs. 4(b) 4(c) and 4(d), the estimated coherence results using a 3×3 Boxcar estimation, ADD and BDD are shown. Figs 4(e) and 4(f) illustrates the ability of anisotropic diffusion to provide a selective smoothing of the processed image. In Figure 5, the histogram of coherence magnitude over ERS dataset and for the three techniques are presented. It is clear that for ADD and BDD, the estimated coherence is much more lower for low coherence values as the histograms are shifted to the left compared to the one obtained with the Boxcar. However, from the ADD filtered image, we observe that a lot of small details are blurred together, leading to biased high coherence estimations. This is due to the difficulty of estimating the true gradient angle in these small areas. For the BDD, this problem does not occur even if in water areas, the gradient values and angles bring false information and lead to formation of high coherence artifacts.

This is confirmed by Figure 6 which plots the coherence magnitude along the red and green profiles (see Fig.4(a)) for ADD,BDD and Boxcar Estimation. From Fig.6(a), we can observe the ADD technique provides the lowest coherence variability in the lake area among the three techniques. But, from Fig. 6(b), we can observe that when facing small features like the river, it provides a much more higher estimation than BDD and Boxcar. In this case, BDD gives an effective estimation while preserving the spatial resolution with sharp transitions between high and low coherence areas (transitions from and to the river area).

In Fig. 8, the result of BDD and ADD combination are shown. When observing the profiles, we can see that

we successfully combined both advantages of ADD and BDD with low coherence variability in the lakes area (Fig. 8(c)) and preservation of small features such as the river (Fig. 8(d)).

Finally, Figure. 7 shows BDD results compared to a 3×3 boxcar estimation for the ENVISAT-WS dataset where a good accuracy is achieved.
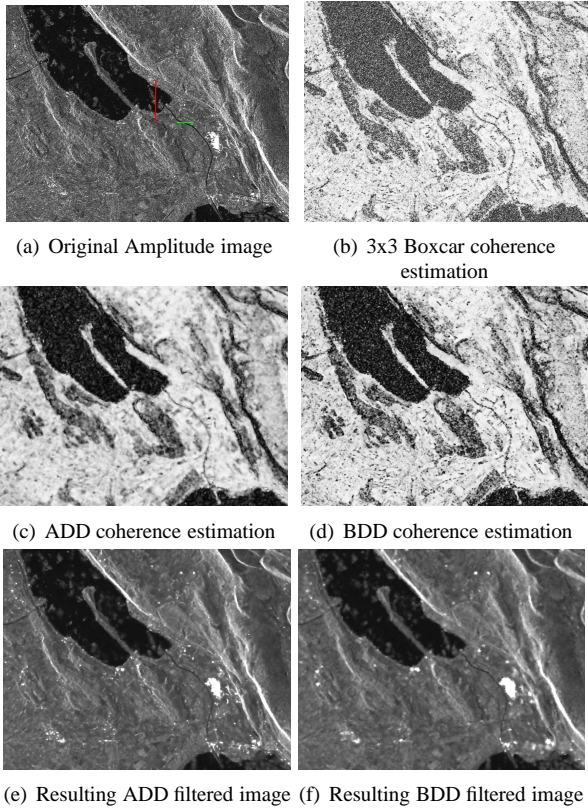

(a) Original Amplitude image

(b) 3x3 Boxcar coherence estimation

(c) ADD coherence estimation

(d) BDD coherence estimation

(e) Resulting ADD filtered image (f) Resulting BDD filtered image

Figure 4. ERS dataset coherence estimation results

(a) 3x3 Boxcar coherence histogram

(b) ADD coherence histogram

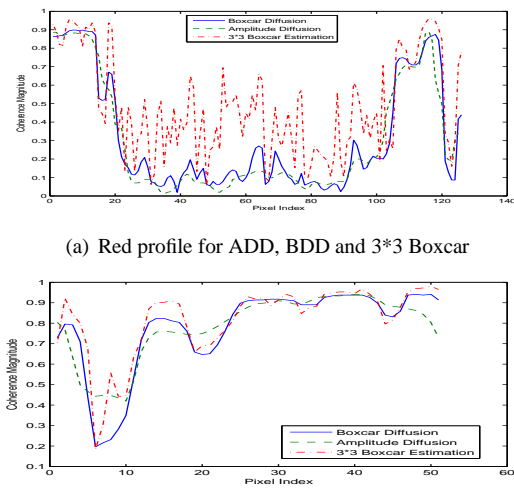(c) BDD coherence histogram

Figure 5. ERS-Dataset coherence histograms

6. SUMMARY

In this paper, two approaches for coherence estimation have been proposed and validated. Indeed, the use of anisotropic diffusion allows the determination a reliable pixel basis for the required spatial averaging in coherence estimation formula. It has been shown that the bias present in another method based on spatial averaging has been highly decreased. Moreover, an original combination of the two methods has been introduced. Such an additional information enabled to take into account cases

(a) Red profile for ADD, BDD and 3*3 Boxcar

(b) Green profile for ADD, BDD and 3*3 Boxcar

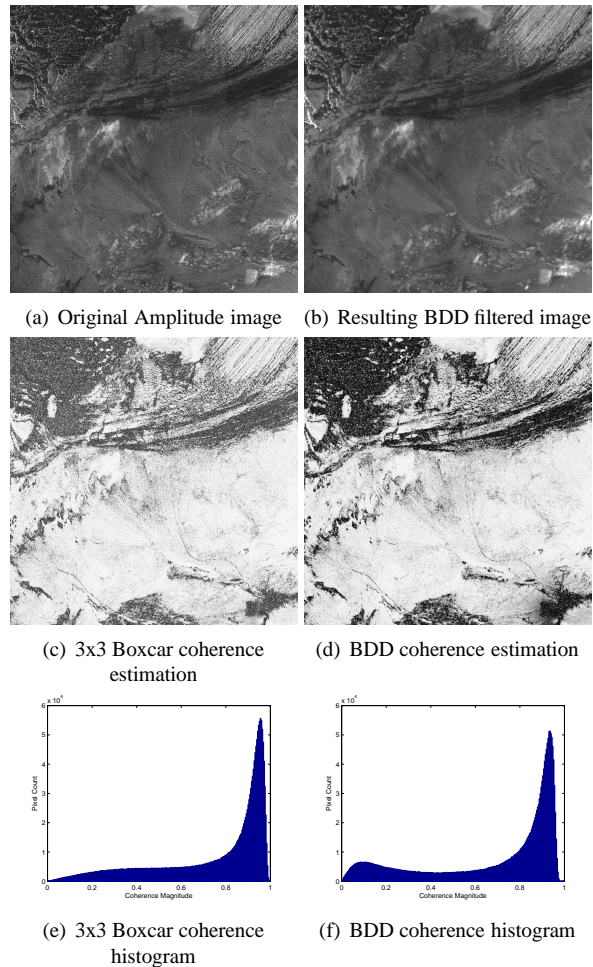*Figure 6. Comparative coherence profile*

(a) Original Amplitude image

(b) Resulting BDD filtered image

(c) 3x3 Boxcar coherence estimation

(d) BDD coherence estimation

(e) 3x3 Boxcar coherence histogram

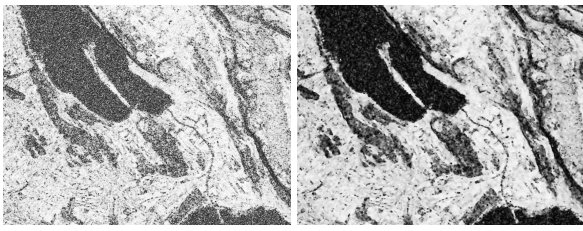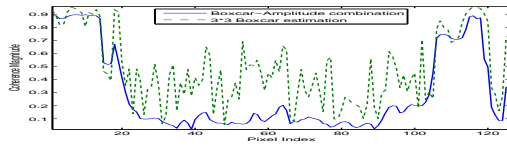(f) BDD coherence histogram

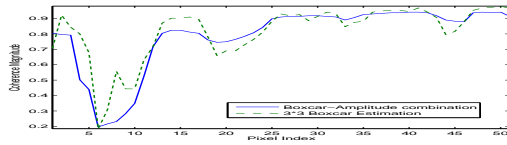*Figure 7. ENVISAT-WS dataset coherence estimation results*

where coherence and amplitude behave oppositely, improving the overall coherence map reliability by taking advantages of both methods. However, it is just a preliminary attempt to solve complex cases and some re-

(a) 3x3 Boxcar coherence estimation

(b) BDD+ADD coherence estimation

(c) Red profile

(d) Green profile

Figure 8. ERS dataset method combination results

search is needed to find an optimal was to combine both techniques. Finally, some quality comparison has been made between ABDD and Boxcar estimation, showing that ABDD provides a high degree of smoothing while preserving a significant spatial resolution.

As a conclusion, we can say the this new technique is already gives promising results but several ways can still be explored to improve the results accuracy.

REFERENCES

1. J. Hagberg, L. Ulander, and J. Askne. Repeat-pass SAR Interferometry over Forested Terrain. *IEEE Transactions on Geoscience and Remote Sensing*, 33:331–340, March 1995.

2. C. Livingstone, A. Gray, R. Hawkins, P. Vachon, T. Lukowski, and M. Lalonde. The CCRS Airborne SAR Systems: Radar for Remote Sensing Research. *Canadian Journal of Remote Sensing*, 21(4):468–491, 1995.

3. E.J.M. Rignot and J.J. van Zyl. Change Detection Techniques for ERS-1 SAR Data. *IEEE Transactions on Geoscience and Remote Sensing*, 31:896–906, July 1993.

4. U. Wegmuller and C. Werner. Retrieval of Vegetation Parameters with SAR Interferometry. *IEEE Transactions on Geoscience and Remote Sensing*, 35:18–24, January 1997.

5. J. Lee, S Cloude, K. Papathanassiou, M. Grunes, and I. Woodhouse. Speckle Filtering and Coherence Estimation of Polarimetric SAR Interferometry Data for Forest Applications. *IEEE Transactions on Geoscience and Remote Sensing*, 41(10):2254–2263, 2003.

6. M. Born and E. Wolf. *Principles of Optics: Electromagnetic Theory of Propagation, Interference and Diffraction of Light*. Pergamon Press, Elmsford, NJ, USA, 1985.

7. R. Touzi, A. Lopes, J. Bruniquel, and P. Vachon. Coherence Estimation for SAR Imagery. *IEEE Transactions on Geoscience and Remote Sensing*, 37(1):135–149, 1999.

8. M. Seymour and I. Cumming. Maximum Likelihood Estimation for SAR Interferometry. In *International Geoscience and Remote Sensing Symposium IGARSS'94, Pasadena*, volume 4, 1994.

9. A. Monti Guarnieri and C. Prati. SAR Interferometry: A "Quick and Dirty" Coherence Estimator for Data Browsing. *IEEE Transactions on Geoscience and Remote Sensing*, 35(3):660–669, May 1997.

10. P. Perona and J. Malik. Scale-Space and Edge Detection Using Anisotropic Diffusion. *IEEE Transactions on Pattern Analysis and Machine Intelligence*, 12(7):629–639, 1990.

11. M.J. Black, G. Sapiro, D.H. Marimont, and D. Heeger. Robust Anisotropic Diffusion. *IEEE Tansactions on Image Processing*, 7(3), March 1998.

12. J. Weickert. *Anisotropic Diffusion in Image Processing*. B.G.Teubner, 1998.

13. J. Weickert. A Review of Nonlinear Diffusion Filtering. In *Scale-Space Theories in Computer Vision*, pages 3–28. Springer, 1997.

14. S. T. Acton and J. Landis. Multi-Spectral Anisotropic Diffusion. *International Journal of Remote Sensing*, 18(13):2877–2886, January 1997.

15. S. Di Zenzo. A Note on the Gradient of a Multi-Image. *Computer Vision, Graphics, and Image Processing*, 33:116–125, January 1986.

16. G. Sapiro and D.L. Ringach. Anisotropic Diffusion of Multivalued Images with Applications to Color Filtering. *IEEE Transactions on Image Processing*, 5(11), November 1996.

17. H. Scharr and J. Weickert. An Anisotropic Diffusion Algorithm with Optimized Rotation Invariance, 2000.

18. A. Monti Guarnieri, P. Guccione, and Y. Desnos P. Pasquali. Multi-Mode ENVISAT ASAR Interferometry: Techniques and Preliminary Results. In *IEE Proceeding of Radar, Sonar and Navigation*, volume 150, pages 193–200, June 2003.